Multiscale bilateral filtering for improving image quality in digital breast tomosynthesis

Yao Lu,[a] Heang-Ping Chan, Jun Wei, Lubomir M. Hadjiiski, and Ravi K. Samala
Department of Radiology, University of Michigan, Ann Arbor, Michigan 48109

(Received 26 May 2014; revised 12 November 2014; accepted for publication 12 November 2014; published 22 December 2014)

Purpose: Detection of subtle microcalcifications in digital breast tomosynthesis (DBT) is a challenging task because of the large, noisy DBT volume. It is important to enhance the contrast-to-noise ratio (CNR) of microcalcifications in DBT reconstruction. Most regularization methods depend on local gradient and may treat the ill-defined margins or subtle spiculations of masses and subtle microcalcifications as noise because of their small gradient. The authors developed a new multiscale bilateral filtering (MSBF) regularization method for the simultaneous algebraic reconstruction technique (SART) to improve the CNR of microcalcifications without compromising the quality of masses.

Methods: The MSBF exploits a multiscale structure of DBT images to suppress noise and selectively enhance high frequency structures. At the end of each SART iteration, every DBT slice is decomposed into several frequency bands via Laplacian pyramid decomposition. No regularization is applied to the low frequency bands so that subtle edges of masses and structured background are preserved. Bilateral filtering is applied to the high frequency bands to enhance microcalcifications while suppressing noise. The regularized DBT images are used for updating in the next SART iteration. The new MSBF method was compared with the nonconvex total p-variation (TpV) method for noise regularization with SART. A GE GEN2 prototype DBT system was used for acquisition of projections at 21 angles in 3° increments over a ±30° range. The reconstruction image quality with no regularization (NR) and that with the two regularization methods were compared using the DBT scans of a heterogeneous breast phantom and several human subjects with masses and microcalcifications. The CNR and the full width at half maximum (FWHM) of the line profiles of microcalcifications and across the spiculations within their in-focus DBT slices were used as image quality measures.

Results: The MSBF method reduced contouring artifacts and enhanced the CNR of microcalcifications compared to the TpV method, thus preserving the image quality of the structured background. The MSBF method achieved the highest CNR of microcalcifications among the three methods. The FWHM of the microcalcifications and mass spiculations resulting from the MSBF method was comparable to that without regularization, and superior to that of the TpV method.

Conclusions: The SART regularized by the multiscale bilateral filtering method enhanced the CNR of microcalcifications and preserved the sharpness of microcalcifications and spiculated masses. The MSBF method provided better image quality of the structured background and was superior to TpV and NR for enhancing microcalcifications while preserving the appearance of mass margins.
 [http://dx.doi.org/10.1118/1.4903283]

Key words: digital beast tomosynthesis, regularization method, multiscale decomposition, bilateral filtering, iterative reconstruction, microcalcification

1. INTRODUCTION

Digital breast tomosynthesis (DBT) is a new imaging modality that utilizes limited-angle computed tomography technology to provide quasi-three-dimensional (3D) structural information of the breast. It has been demonstrated that DBT can reduce tissue overlap and improve the differentiation of normal tissue and suspicious masses. DBT holds strong promise to improve sensitivity for detecting subtle mass lesions compared to mammography.[1–20]

DBT reconstruction can be modeled as a limited-angle cone-beam tomographic problem. DBT system acquires a small number of low-dose x-ray projections of the breast at different projection angles over a limited angular range. The dose used for each projection view is a small fraction of that used in a conventional mammogram and detector noise is added to each projection. The noise level in the DBT projection images is therefore high. In addition, because the projection data are acquired only from a limited angular range, tomosynthesis reconstruction is a severely ill-posed problem. When the tomosynthesized slices are reconstructed from the projection view images, the noise is propagated to the reconstructed volume because of the underdetermined linear system of DBT. The noise affects the visibility and detectability of subtle microcalcifications (MCs) in the reconstructed DBT images.

Regularization is an effective technique to suppress image noise. However, breast images contain subtle features and structured textural background that are more complex than images of natural scenes. These subtle features include MCs, ill-defined or spiculated mass margins, and normal fibrous tissue, ducts, and vasculatures. A major challenge of implementing regularization in DBT reconstruction is to preserve the image quality of significant features and other tissue structures while reducing noise. Subtle MCs that have low contrast may be inadvertently treated as noise and smoothened. The ill-defined margins and spiculations of masses may be distorted or blurred. This will reduce their conspicuity and may cause misdiagnosis of subtle spiculated masses.

Both linear and nonlinear noise regularization methods have been widely used in general image processing field to suppress image noise. A number of regularization methods and noise models have been designed based on the image data and the purpose of image processing. Conventional linear filtering is sufficient to remove additive Gaussian white noise.[21] However, noise smoothing filters will also remove high frequency components in the image data, thus failing to preserve the edges and other texture structures. Various nonlinear noise regularization techniques have been studied for removing noise while preserving edges.[22–26] These nonlinear regularization techniques use the property of edges to estimate their locations and try to navigate filtering across the edges. The physical features of the image data are therefore important for the success of denoising.

Several noise suppression techniques have been proposed for DBT reconstruction. The gradient-based regularization method such as the total variation method was shown to be an efficient method to preserve edges of relatively high-contrast signals in tomosynthesis reconstruction.[27,28] The compressive sensing method with gradient-based penalty term was used for MC enhancement[29] or radiation dose reduction[30] in DBT. The anisotropic diffusion type method was used to improve image quality of DBT reconstruction for MC detection in the spatial domain.[31–33] The iterative penalized maximum likelihood method with an edge-preserving generalized Huber penalty function[34] was used for improving contrast-to-noise ratio (CNR) or detectability of MCs in DBT. All these previous methods intend to enhance MCs by suppressing noise. However, most existing regularization methods for DBT reconstruction are designed for general image applications and are driven by local gradient. These methods work well for strong edges and textures which have good features for the singularity indicator. Although they can successfully enhance the contrast of MCs and reduced noise, they may not preserve the quality of mass margins and subtle tissue structures because of their low gradient edges.

Previously, we developed anisotropic diffusion-based methods to selectively apply regularization to different categories of pixels. The pixels were automatically classified into two categories, potential signals and background noise based on the local gradient[31] or the contrast-to-noise ratio.[32] Different degrees of regularization were applied to potential signal locations and noise locations separately. No regularization or lower degree of regularization was applied to the potential signal locations to preserve potential signals, while higher degree of regularization was applied to the background to smooth noise. The diffusion-based methods were effective to improve image quality of MCs, however, they may treat mass margins and spiculations as background noise because of their small gradients and low contrast, thereby blurring these important features. To preserve the image quality of background tissue structures, we developed a multiscale regularization method for DBT reconstruction.[35] A DBT slice was decomposed into different scales via wavelet transform. No regularization was applied to the component at the coarsest scale. Soft thresholding denoising was applied at the other scales. To enhance the contrast of MCs, we used a combination of specific lesion characteristics of MCs including CNR, size, shape, and edge gradient to search for potential signals, and the wavelet coefficients at the locations of the potential MCs are excluded from soft thresholding. Since no regularization was applied at the potential signal locations, when a pixel was determined to be a part of a potential signal, its CNR would be enhanced relative to the smoothened background in the regularized image. To avoid creating false signals in the reconstruction, a more adaptive regularization method without the selection strategy of the potential signals from background noise is needed.

In this study, we developed a new multiscale bilateral filtering (MSBF) method for iterative DBT reconstruction to improve the CNR of MCs without compromising the quality of masses and soft tissue background structures.[36] The multiscale structure of DBT data was exploited to preserve the image quality of mass margin, spiculations from masses and architecture distortions, and normal tissue structures while bilateral filtering was designed to enhance MCs globally. The MSBF method was used in conjunction with the simultaneous algebraic reconstruction technique (SART) in our implementation for DBT reconstruction. However, in principle, the MSBF method does not depend on specific iterative reconstruction techniques. The performance of the new regularization technique was compared with that of the nonconvex total p-variation regularization method (TpV)[29] and reconstruction with no regularization (NR). The performances of the three methods in terms of the CNR of MCs and the sharpness of subtle signals and spiculations in terms of the full width at half maximum (FWHM) were quantitatively compared.

2. MATERIALS AND METHODS

2.A. Breast tomosynthesis system

A GE prototype GEN2 DBT system in the breast imaging research laboratory at the University of Michigan was used to acquire DBT scans in this study. The imaging geometry of this DBT system is illustrated in Fig. 1. The distance from the x-ray focal spot to the fulcrum of rotation is 64 cm, and the x-ray source rotation plane is parallel to the chest wall and perpendicular to the detector plane. The system has a CsI phosphor/a:Si active matrix flat panel digital detector with a matrix size of 1920×2304 pixels and a pixel pitch

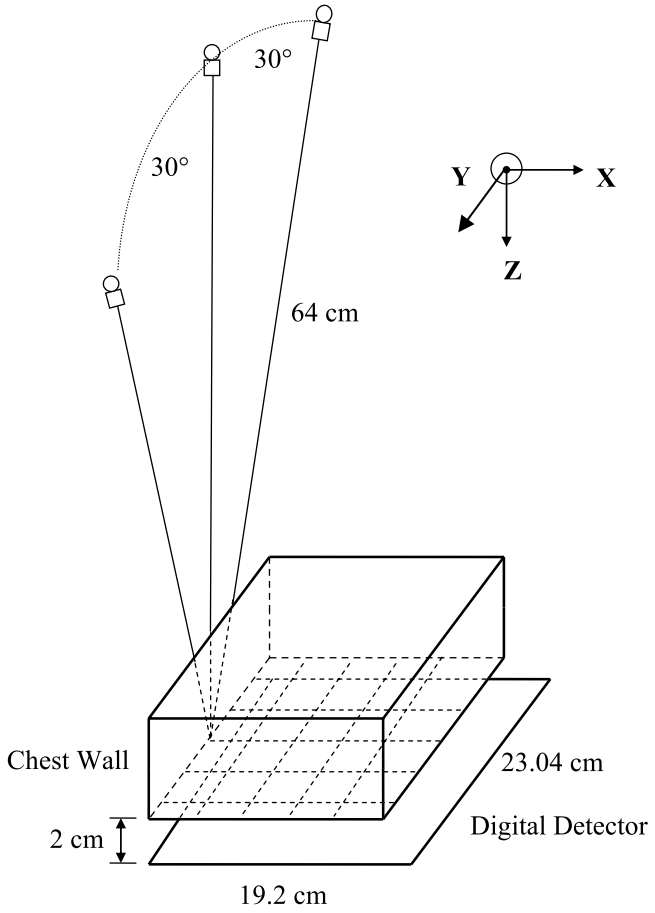

FIG. 1. Geometry of the GE prototype GEN2 digital breast tomosynthesis system used in this study. X-direction is parallel to the tube rotation axis, Y-direction is parallel to the x-ray source motion direction, and Z-direction is the depth direction.

of 0.1×0.1 mm. The digital detector is stationary during image acquisition. The system uses a step-and-shoot design and acquires projection view (PV) images from a total of 21 angles in 3° increments over a ±30° range in less than 8 s. The DBT system uses an Rh-target/Rh-filter x-ray source for all breast thicknesses.

2.B. Simultaneous algebraic reconstruction technique

SART was used for DBT reconstruction in this study.[37] SART is an iterative reconstruction algorithm which can be easily adapted to different imaging geometries. The linear attenuation coefficient of each voxel is updated simultaneously using all rays in one projection. The number of imaged volume updates in one SART iteration is equal to the number of projections. The details of our implementation of the SART and its use with other regularization methods have been discussed previously.[31,32,38]

In our reconstruction, the voxel dimensions of the imaged volume in both the X and Y directions were chosen to be 0.1 mm, the same as the pixel pitch of the detector. The slice spacing in the Z direction was chosen to be 1 mm. A ray-tracing method similar to the Siddon algorithm was employed to calculate the contribution of each voxel to the forward projection.[39] Logarithmic transformation was applied to the raw pixel intensities of the PV image before reconstruction. The projection model assumed a monoenergetic x-ray source and ignored the effects of scattering and beam hardening, similar to the approach by Wu *et al.*[3,40]

2.C. Multiscale bilateral filtering

SART is expected to converge to a weighted least square solution of the DBT reconstruction problem,[41] which, however, is not stable. The noise in the projection views is propagated into the reconstructed image volume and the DBT image noise is magnified with increasing number of iterations.

Breast images contain structures and potential signals with a wide range of spatial frequency contents. Masses and structured tissue background have relatively low-frequency content, and MCs and noise have relatively high-frequency content. To preserve the image quality of masses and breast tissue in the low frequency bands when suppressing noise in the high frequency bands, we use multiscale transform to decompose a DBT slice into different scales, which facilitates the application of different degrees of regularization to the different scales.

2.C.1. Laplacian pyramid decomposition

The Laplacian pyramid decomposition (LPD) method decomposes data into different frequency bands with a multi-scale structure. It was first introduced as an image compression scheme by Burt and Adelson.[42] In medical imaging field, LPD has been used for image enhancement in radiography.[43–47] We previously evaluated the effect of LPD on the detection of MCs on digitized mammograms[43] and masses on full field digital mammograms.[45] The Laplacian pyramid is a sequence of difference images $L_0,L_1,\ldots,L_{n-2}$. Each is the difference between two consecutive levels of the Gaussian pyramid $G_0,G_1,\ldots,G_{n-1}$, where G_0 is the original image. Given a positive real number α, let w_α be a 5×5 Laplacian filter as the tensor product of a one-dimensional Laplacian filter

$$\left(0.25-\frac{\alpha}{2},0.25,\alpha,0.25,0.25-\frac{\alpha}{2}\right), \tag{1}$$

and its transpose. Each subsequent level of the Gaussian pyramid in the decomposition tree is then generated as follows:

$$G_{i+1} = D[G_i \otimes w_\alpha], \tag{2}$$

$$L_i = G_i - \mathrm{EXPAND}[G_{i+1}], \tag{3}$$

for $i = 0,1,\ldots,n-2$, where D is the downsampling operator by a factor of 2, $\otimes$ is the convolution operator, and the pixel value at (s,t) of the upsampled image $\mathrm{EXPAND}[G_{i+1}]$ is defined by

$$\mathrm{EXPAND}[G_{i+1}](s,t) = 4\sum_{k=-2}^{2}\sum_{l=-2}^{2} w_\alpha(k,l)G_{i+1}\left(\frac{s-k}{2},\frac{t-l}{2}\right). \tag{4}$$

The n-level decomposition tree $\{L_0,L_1,\ldots,L_{n-2},G_{n-1}\}$ can be used to recover the original image as follows:

$$G_i = L_i + \text{EXPAND}[G_{i+1}], \tag{5}$$

for $i = 0,1,\ldots,n-2$. Details of the decomposition and reconstruction processes can be found in the literature.[42]

2.C.2. Bilateral filtering

Using the LPD, the individual DBT slices after each iteration are first decomposed into different frequency bands. The mass margins and spiculations fall mainly into the low-frequency bands while MCs, edges, and noise fall mainly into the high-frequency bands. To preserve masses and structured tissue background while removing noise, no regularization is applied to the low-frequency band (G_{n-1}) while high degrees of regularization are applied to the high-frequency bands ($L_0,L_1,\ldots,L_{n-2}$). In the high-frequency bands, MCs may be distinguished from noise by either stronger gradient or larger size. For high-contrast MCs, strong gradient is a good indicator of potential signals. For subtle MCs, the size of the signals, in addition to the local gradient, has to be considered to suppress noise while preserving potential signals.

Bilateral filtering is a nonlinear filter which exploits both geometric uniformity in the spatial domain and intensity similarity in the range.[48,49] Bilateral filtering has a fundamental relationship with the Beltrami flow,[50] local mode filtering,[51] Bayesian approach,[52] anisotropic diffusion,[25,53] and robust estimation.[24] Bilateral filtering has been widely applied to denoising and image enhancement for general image processing, computer graphics, and medical imaging.[26,54–56] In general, bilateral filtering performs as a nonlinear smoothing operator B defined by

$$B[I](x) = \frac{1}{C_x} \sum_{x' \in S_x} G_{\sigma_d}(\|x - x'\|) G_{\sigma_r}(|I(x) - I(x')|) I(x'), \tag{6}$$

where S_x is a set of neighborhood points around the pixel with its coordinate denoted as vector $\boldsymbol{x}$, $\|\boldsymbol{x}-\boldsymbol{x}'\|$ is the Euclidean distance between two pixels $\boldsymbol{x}$ and $\boldsymbol{x}'$, $|I(\boldsymbol{x})-I(\boldsymbol{x}')|$ is the absolute difference in pixel values at $\boldsymbol{x}$ and $\boldsymbol{x}'$, respectively, G_σ is a Gaussian function with standard deviation σ, the weight of spatial distribution $\{G_{\sigma_d}(\|\boldsymbol{x}-\boldsymbol{x}'\|) : \boldsymbol{x}' \in S_x\}$ is called a domain filter and the weight of intensity variation distribution $\{G_{\sigma_r}(|I(\boldsymbol{x})-I(\boldsymbol{x}')|) : \boldsymbol{x}' \in S_x\}$ is called a range filter, σ_d and σ_r are the standard deviations of the domain filter and range filter, respectively, and C_x is a normalization factor defined by

$$C_x = \sum_{\boldsymbol{x}' \in S_x} G_{\sigma_d}(\|\boldsymbol{x}-\boldsymbol{x}'\|) G_{\sigma_r}(|I(\boldsymbol{x})-I(\boldsymbol{x}')|). \tag{7}$$

Note that the domain filter and the range filter are shift-variant, which cause high computational cost for the nonlinear filtering.

With the multiscale structure from the LPD, bilateral filtering is applied to the high frequency bands while no regularization is applied to the low frequency band, the following multiscale bilateral filtering scheme is obtained. Given an n-level LPD tree $\{L_0,L_1,\ldots,L_{n-2},G_{n-1}\}$, the multiscale bilateral filtered image $\tilde{G}_0$ can be reconstructed as follows:

$$\tilde{G}_{n-1} = G_{n-1}, \tag{8}$$

$$\tilde{G}_i = B[L_i] + \text{EXPAND}[\tilde{G}_{i+1}], \tag{9}$$

where $i = 0,1,\ldots,n-2$.

Multiscale bilateral filtering regularization is applied to the DBT images slice by slice at the end of each SART iteration and the denoised DBT volume is used for the next SART iteration. A flow chart of the SART-based DBT reconstruction using multiscale bilateral filtering is shown in Fig. 2.

2.D. Figures of merit

To evaluate the image quality of the reconstructed MCs and masses, the CNR of selected signals and the FWHM of selected line profiles intersecting the MCs or mass spiculations on the reconstructed DBT slices were measured and compared among the regularized reconstruction methods.

The normalized line profile and its FWHM in the focal plane of a signal were used to measure the in-plane image sharpness. For MCs, two line profiles approximately intersecting the center of the calcification in the direction perpendicular to the chest wall (X) and the direction parallel to the chest wall or the x-ray source motion direction (Y) were chosen. Each line profile was obtained by averaging one to three parallel lines to reduce noise, depending on the size of the MC being analyzed. For spiculations, the centerline of a spiculation was rotated to the vertical direction using linear interpolation, then a line profile was obtained by averaging three neighboring horizontal lines intersecting the spiculation. The baseline of each line profile was estimated

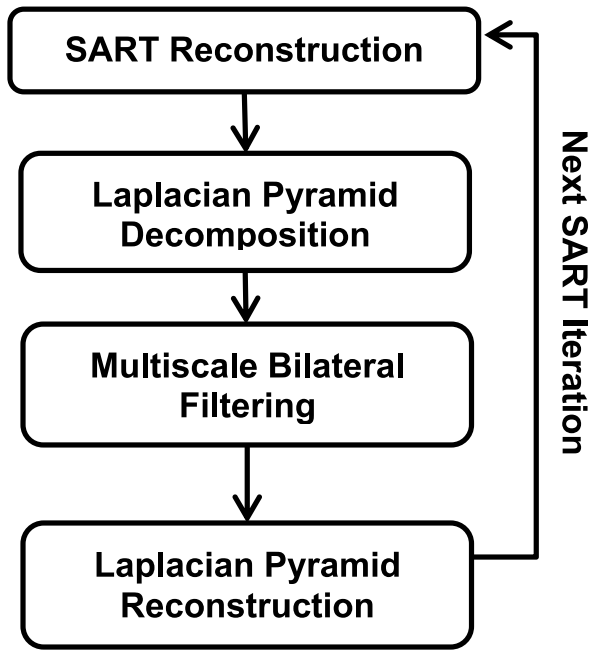

FIG. 2. Flow diagram of SART-based DBT reconstruction with multiscale bilateral filtering regularization.

from a linear fit to the background pixels in the neighborhood of the object of interest and subtracted from the line profile. A Gaussian function was used for curve fitting of the background-corrected line profile. The FWHM of the line profile is defined as

$$\mathrm{FWHM} = \left(2\sqrt{2\ln 2}\right)\sigma, \tag{10}$$

where σ is the standard deviation of the fitted Gaussian function.

The CNR value was used to measure the contrast of the MC relative to the background noise in a region of interest (ROI) neighboring the MC. The CNR value is defined as

$$\mathrm{CNR} = \frac{\bar{I}_{\mathrm{ROI}} - \bar{I}_{\mathrm{BG}}}{\sigma_{\mathrm{BG}}}, \tag{11}$$

where $\bar{I}_{\mathrm{ROI}}$ is the mean pixel value in a selected ROI centered at the center of the MC, $\bar{I}_{\mathrm{BG}}$ is the mean pixel value in an ROI of a neighboring background region located on the same slice, and σ_{BG} is the standard deviation of pixel values in the background ROI. The ROI for a signal was selected as a 3×3-voxel square for large MCs and 1×1-voxel square for small MCs. The ROI for the background noise for a given MC was selected as a 40×40-voxel square from a relatively uniform region near the MC with gray levels similar to those surrounding the MC.

2.E. Study conditions

SART with MSBF regularization was applied to DBT of breast phantoms and human subjects. The MSBF method was compared with the nonconvex TpV regularization[29] and SART without regularization. The TpV method was implemented following the pseudocode and the parameters described by Sidky *et al.*[29] The p value was chosen to be 0.8, which was also used in our previous study.[31] The comparisons were performed over five iterations of SART and the images after five iterations were analyzed. The reconstruction volume was initialized to have a uniform value of zero.

A three-level decomposition ($n = 3$) was performed for the LPD in this study, and the parameter α of the Laplacian filter used for the LPD in Eq. (1) was selected as 0.375 empirically. The Laplacian filter with $\alpha = 0.375$ is shown in Fig. 3. There are two parameters related to the performance of the bilateral filtering. The width of the range filter, as determined by the standard deviation σ_r, controls the weights in the range. When σ_r is too large, the range filter is relatively smooth and the bilateral filter will behave like a spatial Gaussian filter. When σ_r is too small, the bilateral filter will be dominated by the range filter and may behave like a conventional gradient-based diffusion method. In general, the choice of σ_r should be related to the local noise level, such that bilateral filtering will reduce noise and preserve the signals above the noise level. In our application, the noise level is estimated adaptively to the individual DBT volume as follows. The breast parenchymal region on each DBT slice is split into nonoverlapping 20×20 pixel ROIs. The root-mean-square (RMS) variation of pixel values within each

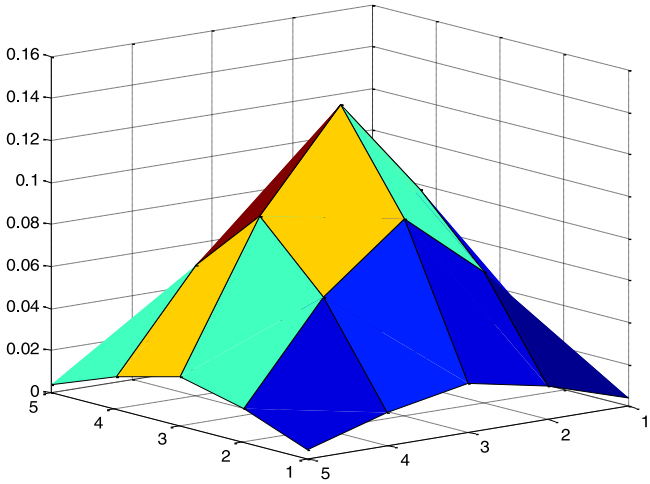

FIG. 3. Plot of the two dimensional tensor product Laplacian filter when $\alpha = 0.375$.

ROI, after the background level is subtracted, is calculated and averaged over all ROIs on the same slice to estimate the noise level. To avoid discontinuity between neighboring slices, the RMS values are averaged over all slices and the σ_r value for the whole volume is set to be this mean RMS value. Therefore, the value of σ_r is automatically calculated for each DBT volume in our implementation of the bilateral filter. The calculated value of σ_r falls into the range of [0.005, 0.02] after the voxel values of the reconstructed slices are normalized to the range of [0, 1].

For the domain filter, the width of the Gaussian filter is controlled by the standard deviation σ_d, which determines how many neighboring points are involved in the weighted average. The σ_d value is related to the signal scale. The optimal regularization parameter σ_d is selected experimentally, as shown below.

2.F. Breast phantoms

The modular breast simulating phantom[57] consisted of a stack of five 1-cm-thick 50% adipose/50% glandular heterogeneous slabs that mimic the composition and parenchymal pattern of the breast (CIRS, Inc.). We arranged the slabs in the stack in four different orders and each was imaged as a different phantom. Clusters of calcium carbonate specks of three nominal size ranges (0.25–0.30 mm, 0.18–0.25 mm, and 0.15–0.18 mm) (CIRS, Inc.) were used to simulate MCs of different conspicuity levels (high, median, and subtle contrast, respectively). Several clusters of each contrast group were sandwiched at random locations between the slabs in each phantom. The exposure conditions for all phantoms were fixed at Rh/Rh 29 kV and a total of 50 mAs for the 21 PVs, which was estimated to produce the same mean glandular dose (about 1.1 mGy) as a single-view digital mammogram for a breast of similar composition and thickness as the phantom using the standard dose mode in a GE essential digital mammography system.

For each phantom, we randomly selected three sets of specks, four samples for each set, representing high, median,

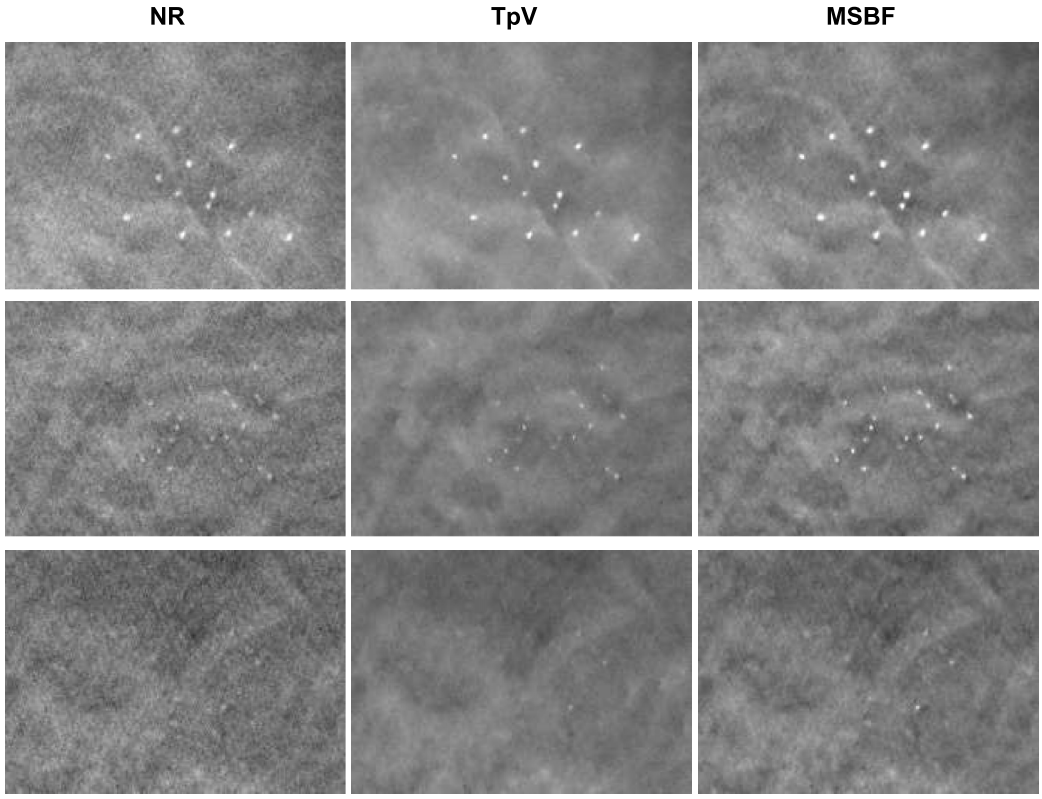

FIG. 4. Examples of simulated MC clusters of three contrast groups in the breast phantoms: (first row) high contrast, (second row) median contrast, (third row) low contrast, from which one of the 16 MC samples were selected for the analysis of CNR and FWHM. First column: NR. Second column: TpV, with $p = 0.8$. Third column: MSBF, where $\sigma_d = 2$ and results after five iterations were shown. The same window and level settings were applied to images in the same row.

and subtle contrast MCs, respectively, from the different groups of simulated MC clusters. In total, we analyzed 16 samples from 16 clusters in the four phantoms for each contrast group. The same three sets of simulated MCs were used for the analysis of CNR and FWHM in the phantom images reconstructed under the various conditions and parameter settings. Examples of clusters of the three size ranges are shown in Fig. 4.

2.G. Human subjects

DBT scans of human subjects were collected with IRB approval and written informed consent. Patients who were recommended for biopsy of a suspicious lesion in the breast were eligible. Because the true size of a given MC in the breast is not known and analysis based on size grouping is difficult, only a few individual MCs of a range of conspicuity were quantitatively analyzed for demonstration purposes. The MCs and mass spiculations were chosen from two DBT of human subjects containing a malignant spiculated mass, one with and the other without MCs. Other human subject images were used only for subjective visual comparisons.

3. RESULTS

3.A. Breast phantoms

The dependence of the CNR of the simulated MCs in the reconstructed images on the σ_d of the domain filter is shown in Fig. 5. The σ_r value of the range filter was set to be the RMS values adaptively determined for each DBT slice, as described above. For a given contrast group, the CNR was averaged over the 16 samples, and the standard deviation is shown as error bars. It is seen that the mean CNR increased with increasing σ_d at small σ_d values. The CNR reached a broad maximum and decreased gradually when the σ_d value

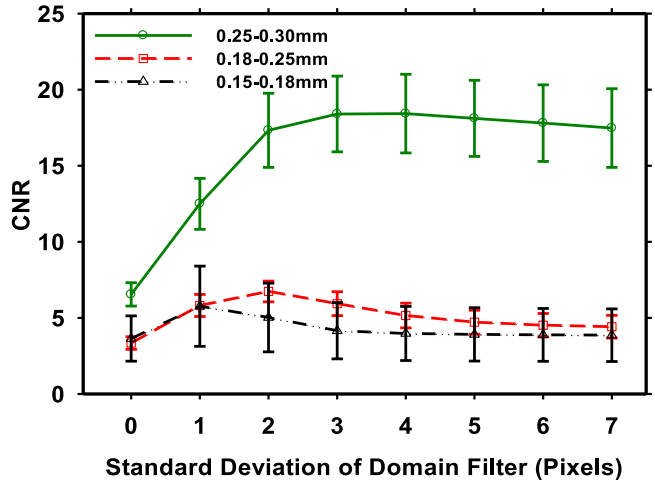

FIG. 5. Dependence of CNR values on the standard deviation of domain filter σ_d for three different groups of simulated MCs. Each CNR value was obtained by averaging 16 simulated MCs from 16 clusters of a given nominal size in four breast phantoms, and the error bars indicated one standard deviation of the 16 measurements.

continued to increase. The σ_d value that provided the highest CNR varied among the three contrast groups and fell in the range of 1–3 pixels. The σ_d value approximately indicates the minimal signal scale that the filtering method preserves. The larger the nominal size of the signals, the larger the optimal σ_d value was under the conditions studied.

The average FWHM values of the gray-level line profiles of the selected MCs in DBT of the breast phantoms were plotted in Fig. 6. Because of the noisy images and the variations of the MC sizes in each size group, the error bars were very wide. There was no clear trend of the FWHM values in either the X- or the Y-directions. For the MCs in all three contrast groups, the FWHM values were comparable for different domain filters, and they were comparable to the reconstruction with NR, which was equivalent to the data points at $\sigma_d = 0$.

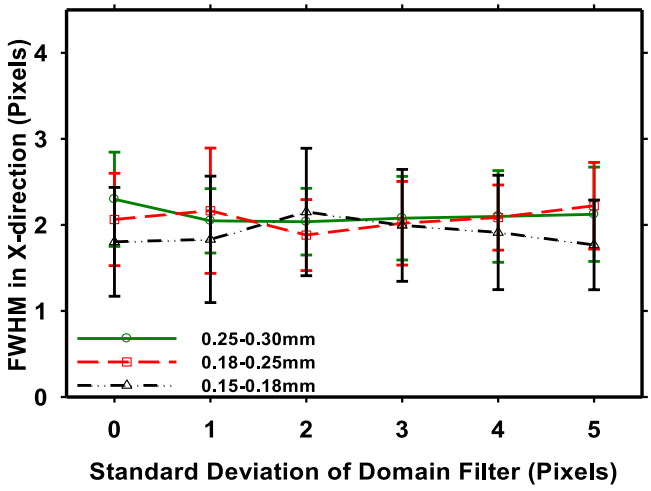

(a)

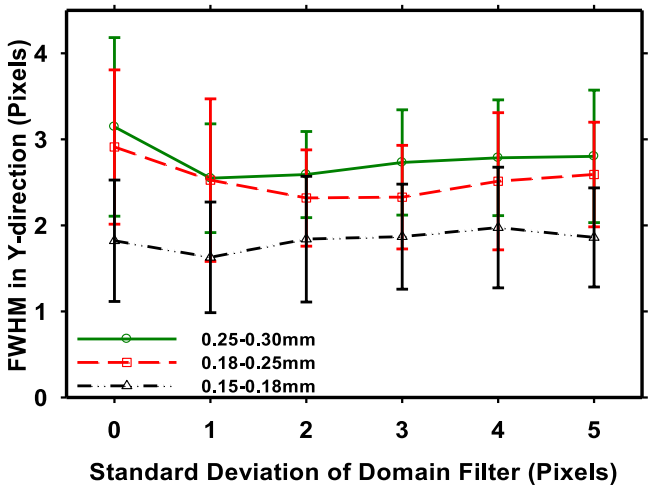

(b)

FIG. 6. Dependence of FWHM values on the standard deviation of domain filter σ_d for three different groups of simulated MCs, where results after five iterations were shown. Each FWHM value was obtained by averaging 16 simulated MCs from 16 clusters of a given nominal size in four breast phantoms, and the error bars indicated one standard deviation of the 16 measurements. (a) X-direction: perpendicular to x-ray source motion. (b) Y-direction: parallel to x-ray source motion.

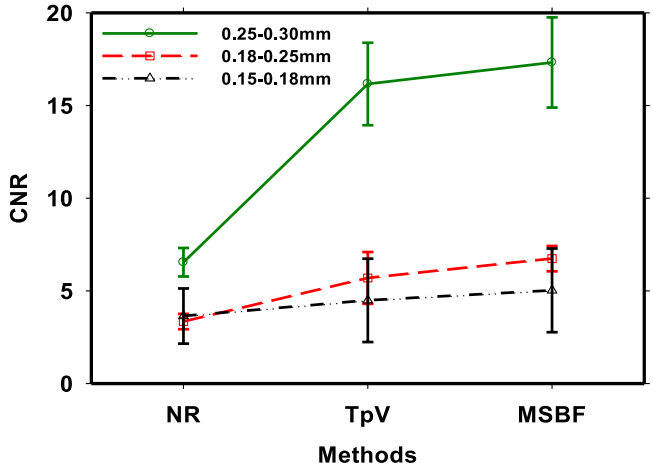

FIG. 7. Comparison of CNR values obtained from three different reconstruction methods for three different groups of simulated MCs. Each CNR value was obtained by averaging 16 simulated MCs from 16 clusters of a given nominal size in four breast phantoms, and the error bars indicated one standard deviation of the 16 measurements. The CNR values at $\sigma_d = 2$ and 5 iterations were shown for MSBF. There were no functional relationships between data points of the three methods. The line connecting the data points of each MC contrast group was plotted to facilitate visual comparison.

We compared the reconstruction results with the TpV method, the MSBF method, and no regularization. The CNR values of the signals from the three contrast groups were shown in Fig. 7. For the MSBF method, the CNR values obtained with $\sigma_d = 2$ were plotted. Both the TpV method and the MSBF method substantially improved the contrast of the signals. In terms of CNR values, the MSBF method was superior to the TpV method and the NR method. On average, the MSBF method achieved 10%–20% higher CNR values than the TpV method and 50%–200% higher CNR values than the NR method.

The in-plane signal sharpness in terms of the FWHM of the MCs in the X- and Y-directions were compared in Figs. 8(a) and 8(b), respectively. The σ_d value was again fixed at 2 in the MSBF method for all contrast groups. The trend of the FWHM values among the three methods was similar in both the X-direction and the Y-direction. For high-contrast signals (0.25–0.30 mm group), the TpV method found the signals based on their large gradients, and the reconstructed signals were sharper than the results with no regularization. However, for relatively subtle signals (0.15–0.18 mm group), the TpV method might have smoothened the signals and caused larger FWHM values due to blurring. On average, the FWHM values of the MSBF method were more consistent with those with no regularization, indicating that the MSBF method was more effective in preserving the shape of signals in terms of the FWHM values.

3.B. Human subjects

We applied MSBF regularized SART to DBT of a number of human subject breasts. We visually compared the MCs and the appearance of spiculations and breast parenchyma in the reconstructed images using σ_d value ranging from 1 to 5. When σ_d value is close to 1, the reconstructed images

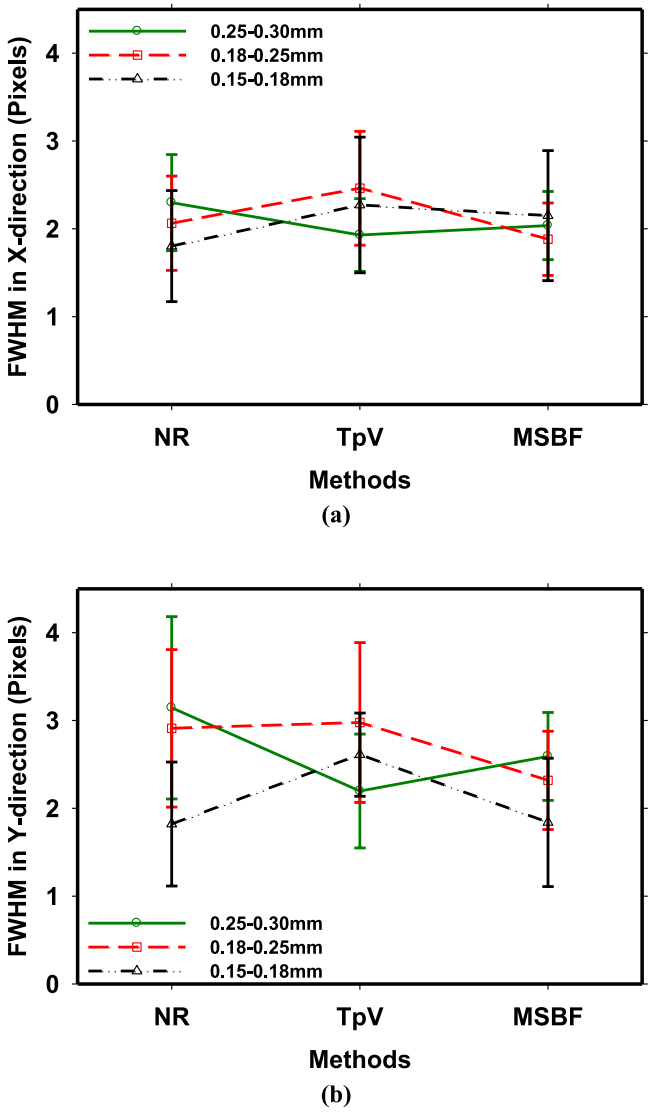

FIG. 8. Comparison of FWHM values obtained from three different reconstruction methods for three different groups of simulated MCs. Each FWHM value was obtained by averaging 16 simulated MCs from 16 clusters of a given nominal size in four modular breast phantoms, and the error bars indicated one standard deviation of the 16 measurements. The FWHM values at $\sigma_d = 2$ and 5 iterations were shown for MSBF. (a) X-direction: perpendicular to x-ray source motion. (b) Y-direction: parallel to x-ray source motion.

appeared noisy and spurious noise points were seen in the reconstructed images. When σ_d value is close to 5, the reconstructed images appeared smooth and some subtle MCs were blurred. In combination with the results of parameter selection study with phantoms described above, we empirically selected the σ_d value as 3 for the domain filter. An example of a cluster of MCs of various sizes from a DBT of a human subject reconstructed with MSBF using different standard deviation of domain filter σ_d is shown in Fig. 9.

Two DBT scans of human subjects containing a malignant spiculated mass, one with and the other without MCs were chosen for quantitative analysis. MCs of three sizes were selected. Figure 10 shows an example of an in-focus DBT slice containing a large spiculated mass and a large number of MCs of various sizes reconstructed using different regularization methods. The slice was located at 2.8 cm above the breast support plate. Three calcifications of different sizes that had their best focused plane on this slice were selected and numbered as shown. Visual comparison of the images indicated that both the TpV [Fig.10(b)] and the MSBF [Fig.10(c)] methods significantly reduced the noise level and preserved the sharpness of the spiculations. However, the TpV method caused *staircasing* (i.e., contouring) artifacts in the soft tissue background, as seen in the ROI in Fig.10(d), and aggravated local discontinuity of the spiculations. No staircasing artifacts were apparent in the MSBF regularized images and the texture of the soft tissue background appeared more natural. The MSBF method was less prone to the discontinuity of the spiculations and provided stronger contrast enhancement for subtle MCs than the TpV method compared to NR. Examples of the low-frequency component and high-frequency component of the same cluster without regularization and with MSBF were presented in Fig. 11. Comparison of the high frequency component (second row) showed that the bilateral filtering substantially suppressed the noise and preserved the important features of the original image.

The CNR values of the selected MCs for the three methods are compared in Fig. 12. In terms of the CNR value, the MSBF method was superior to the TpV and NR methods for MCs of different sizes. The MSBF method achieved 100%–140% higher CNR than the NR method and 20%–60% higher CNR than the TpV method.

The in-plane signal sharpness in terms of the FWHM of the MCs in the X- and Y-directions is compared in Figs. 13(a) and 13(b), respectively. The trends are different than those from analysis of the phantom images, probably because of the large uncertainty with a single measurement. One similar observation was that for small signals (e.g., signal 3), the FWHM might increase due to smoothing if the regularization method mistakenly treated them as noise. However, the CNR might still be improved compared to that without regularization because the noise was reduced, as shown in Fig. 12.

The MSBF method provided better image quality than the TpV method for low contrast spiculations, as illustrated by the examples in Fig. 14. Figure 15 compares the FWHM values of the line profiles perpendicular to the centerlines of the spiculations for the three methods. The FWHMs obtained from the MSBF method were similar to those from the NR method, and both were smaller than those from the TpV method, indicating that the MSBF method better preserved the shape of low contrast structures such as spiculations and fibrous tissue while the TpV method might introduce additional blurring. While the TpV images appeared to be less noisy than the MSBF images, the staircasing artifacts were apparent in the TpV images. In comparison, the MSBF method reduced the noise and enhanced the MCs without changing the parenchymal texture substantially.

4. DISCUSSION

In this study, we designed a regularization framework that exploits the multiscale structure of image features in

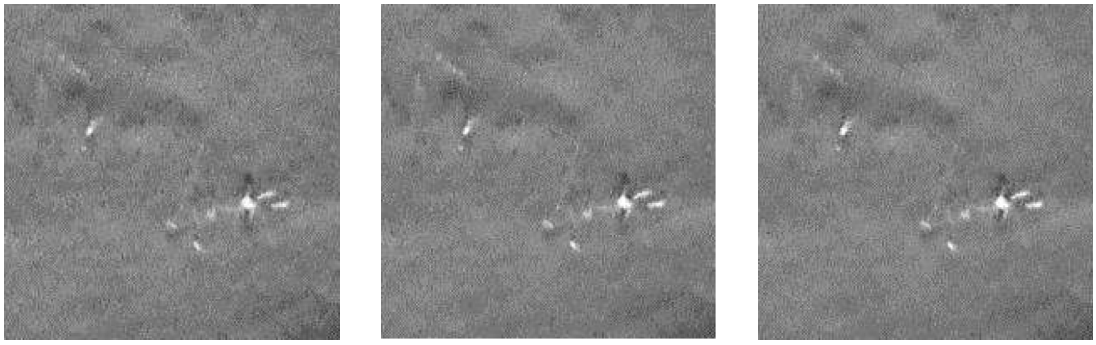

(a) $\sigma_d = 1$ (b) $\sigma_d = 2$ (c) $\sigma_d = 3$

FIG. 9. Example of a cluster of MCs of various sizes from a DBT of a human subject reconstructed with MSBF using different standard deviation of domain filter σ_d. The same window and level settings were applied to the three images.

the breast to suppress noise while preserving subtle mass spiculations and structured tissue background for iterative DBT reconstruction. The multiscale structure is derived by decomposition of the reconstructed data from the current SART iteration and the denoised DBT data serve as input to the next SART iteration. No regularization is applied to the low frequency band to preserve the complex and subtle structured tissues, which prevents the *staircasing* artifact[58] from the TV-type regularization methods. TV-type regularization is useful in enhancing high contrast edges and signals.

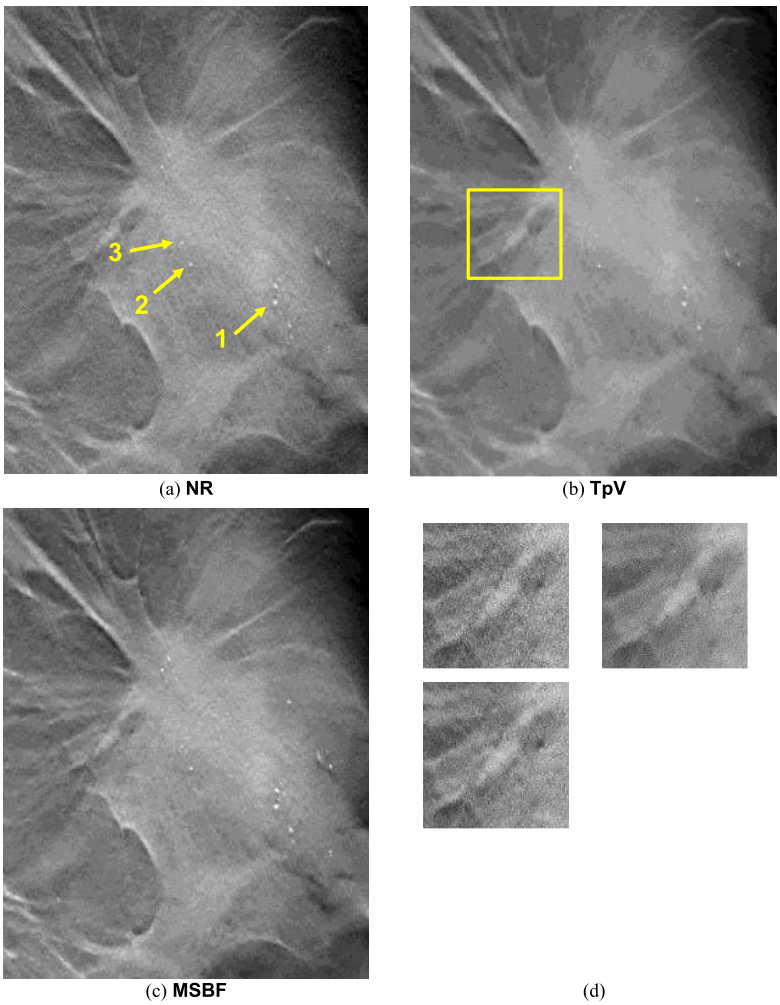

(a) **NR** (b) **TpV**

(c) **MSBF** (d)

FIG. 10. (a) A spiculated mass with MCs of various sizes from a mediolateral–oblique view DBT of a human subject reconstructed without regularization. The in-focus DBT slice for the three selected calcifications is shown. The three selected signals were numbered in approximately decreasing size and contrast. The reconstructed slice using (b) nonconvex TpV ($p = 0.8$) and (c) MSBF ($\sigma_d = 3$) for regularization. All three images were displayed with the same window and level settings. (d) Zoomed-in region of interest (yellow rectangle) at a spiculation in (b) for three different methods: NR (upper-left), TpV (upper-right), and MSBF (lower-left). All three ROI images were displayed with the same window and level settings.

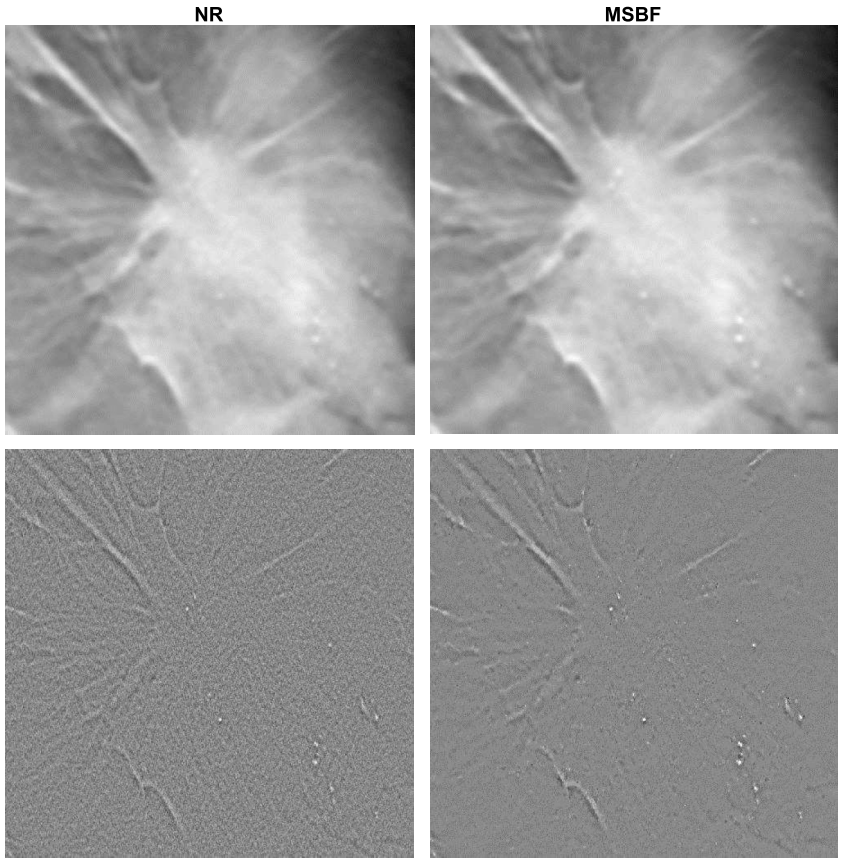

FIG. 11. Examples of the low-frequency component and high-frequency component of a spiculated mass with MCs of various sizes from a mediolateral–oblique view DBT of a human subject after five iterations: (first column) no regularization, (second column) with MSBF. First row: low-frequency components; second row: high-frequency components, MSBF ($\sigma_d = 3$) reduces the noise substantially. Images in the same row are displayed with the same window and level settings.

However, it is difficult to determine a stopping criterion that is appropriate for the complex breast structures over the whole image domain. As a result, TV-type regularization may over-smooth some structures and subtle mass spiculations and create the *staircasing* artifact. For the MSBF method, we experimentally determined that three-level LPD is adequate to separate low frequency structured background and noise (see Fig. 11). For both phantom data and human subject data, the MSBF method removed the noise effectively while enhancing the contrast of MCs and preserving structured background. With human subject data, the ability of MSBF in preserving the subtle mass spiculations was demonstrated. From both FWHM analysis and visual comparison, the MSBF preserved the shape of the signals and structured tissues relatively well in comparison to that of NR. The TpV method was more variable such that it showed a trend to sharpen high-contrast calcifications while blurring low-contrast subtle calcifications and spiculations.

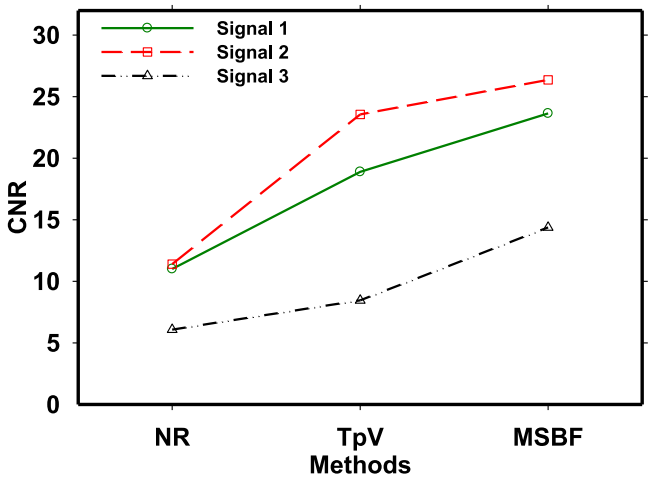

FIG. 12. Comparison of CNR values obtained from three different reconstruction methods for three MCs in Fig. 10.

The multiscale structure decomposition in this study was achieved by the LPD. However, the multiscale decomposition is not limited to LPD and other multiscale analysis methods may work as well. Note that MCs may not have strong directional geometric features; therefore, the directional multiscale analysis method such as wavelet transform or curvelet transform may not have advantages over the LPD method for the purpose of microcalcification enhancement.

Since bilateral filtering is a nonlinear filtering method, the point-to-point weighted average calculation results in high computational cost. Parallel computing, especially GPU computing, is usually employed to alleviate the problem. In our implementation, for a typical DBT volume with

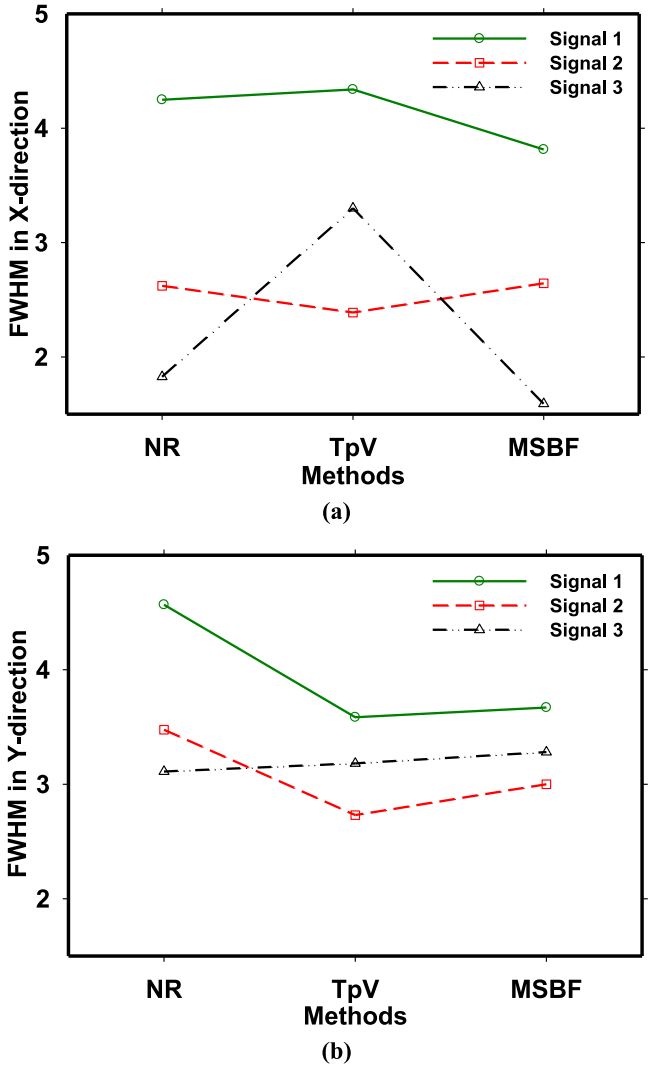

FIG. 13. Comparison of FWHM values obtained from three different reconstruction methods for three MCs in Fig. 10.

dimensions of 1470×2304×61, the bilateral filtering applied to the whole volume caused 6350 s with one computation thread on a CPU of 3.47 GHz and 24 GB of system memory, compared to 5 s on the same workstation using a NVIDIA Tesla C2070 computing processor (6 GB GDDR5 RAM, 448 processing cores). Currently, our SART and LPD have not been implemented on GPU. The total elapse time (SART + LPD + bilateral filtering) for five iterations was 3625 s, which included the input/output time of the image data from/to a network drive at various stages of the process. Compared to the total time, the computational cost of bilateral filtering with GPU is negligible.

In our preliminary exploration of multiscale regularization methods for DBT reconstruction,[35] we used multiscale wavelet decomposition and constrained regularization by a characteristic map which was generated via image feature analysis to identify potential microcalcification locations in the DBT volume. Soft thresholding denoising was applied at the high frequency bands while the wavelet coefficients at the locations of the potential MCs were excluded from soft thresholding. Although this method was found to be effective for MC enhancement, it has the disadvantages that it depends on the accuracy of the characteristic map. Subtle MCs may be preserved at the cost of retaining a large number of potential signal locations, which can become false signals after enhancement. The current method eliminates the need for the characteristic map. With proper selection of the parameters of the bilateral filter, the MSBF method is found to be relatively adaptive to DBT of various parenchymal structures.

We incorporate the MSBF method into the SART framework. In practice, the MSBF method is applicable to any iterative reconstruction method for any imaging geometry. Even for noniterative reconstruction method such as the filtered backprojection (FBP) method, the MSBF could also be employed as a post-processing method to enhance the CNR of MCs in DBT images.

FBP is a popular method for tomographic reconstruction. For the FBP method of DBT reconstruction, an important task is to design the filter, which may depend on many factors such as the tomographic angle, angular increments, and noise of the DBT acquisition. An extensive optimization study is needed in order to achieve good image quality with FBP, as with any reconstruction methods. We have not studied the filter design for the FBP method so that we cannot easily compare SART with MSBF to FBP with MSBF. If other researchers who have a FBP algorithm optimized for DBT reconstruction and are interested in such a comparison, we will make the raw phantom images available to facilitate the comparison.

The clusters of calcium carbonate specks in the breast phantoms have three nominal size ranges, as provided by the manufacturer. The actual size of an individual speck was unknown and it varied even for specks of the same nominal size. To estimate the FWHM of a line profile across a reconstructed speck image, voxels along the line profile of the speck were selected to fit a Gaussian function after removing the background. For large specks, because of the in-plane and out-of-plane blurring from the limited-angle reconstruction, there could be 4–7 voxels along the line profile across the reconstructed speck to fit the Gaussian function. For small specks, the number of voxels along the line profile could be as small as 4. The Gaussian curve fitting was sensitive to noise, especially when there were few points to fit. In such cases, the termination condition of the iterative curve fitting method was adjusted individually to obtain the best fitted curve for the given speck. The noisy curve fitting and the variation in the physical size of the specks resulted in large variances in the FWHM estimations.

The FWHM curves have different patterns in X- and Y-directions (Fig. 6). The FWHM values in the X-direction almost overlapped with each other, while the separation in the FWHM values in the Y-direction were relatively large, especially for the 0.25–0.30 mm and 0.18–0.25 mm groups. This difference may be caused by several factors. Our SART reconstruction assumed monoenergetic x-rays but the x-ray source was polyenergetic. The beam hardening effect[59–61] would introduce streak artifacts, which could contribute to the darker shadows around the MCs in the Y-direction.

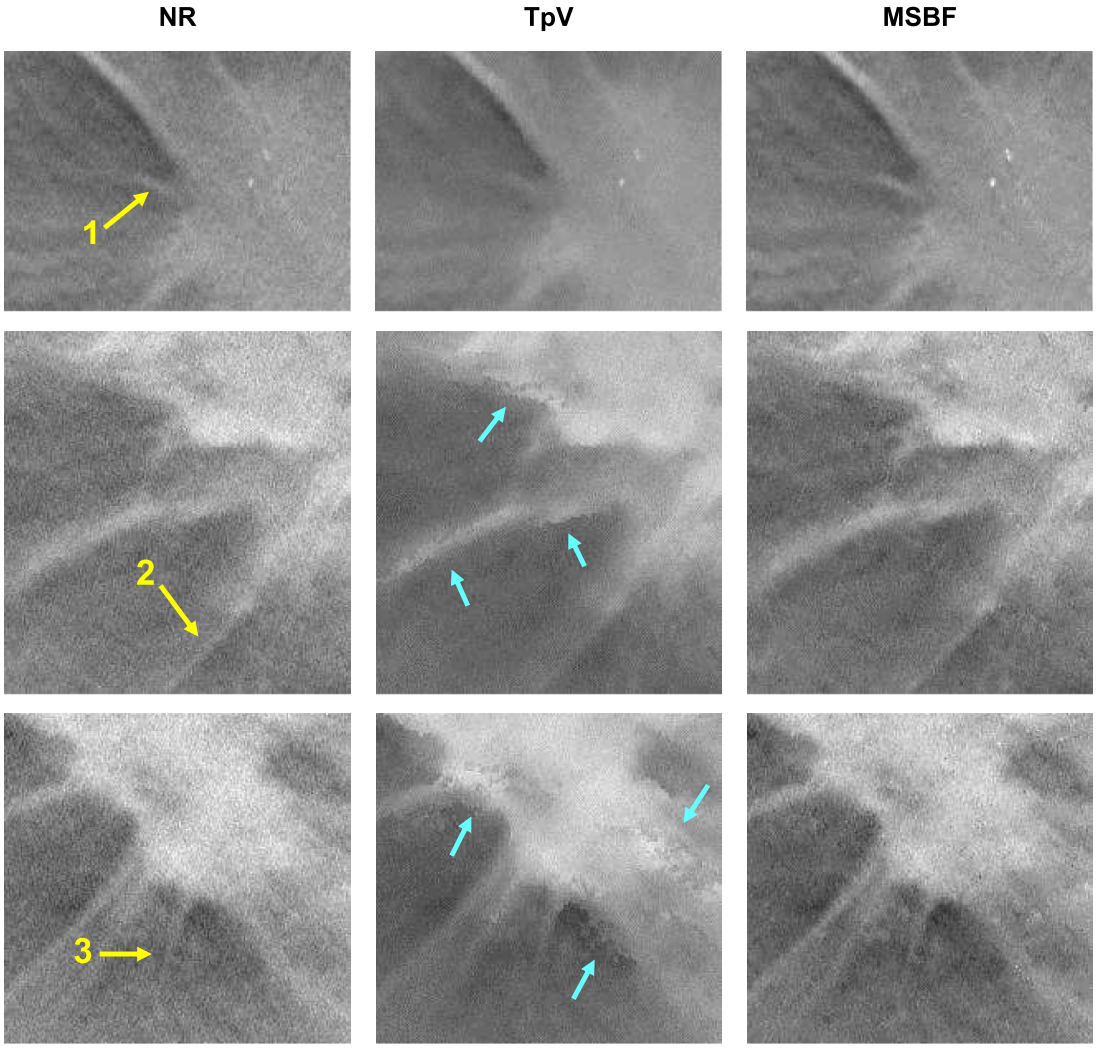

FIG. 14. The regions of interest around three selected subtle spiculations using the NR (left column), TpV (middle column), and MSBF (right column) methods, respectively. The arrows with numbers indicate the spiculations of which the FWHM was analyzed in Fig. 15. The MSBF images ($\sigma_d = 3$) are often noisier than the TpV images, but the contrast of the calcifications in the MSBF images are more enhanced, as demonstrated in the region around spiculation 1. TpV regularization can cause *staircasing* artifacts as seen in the regions around spiculations 2 and 3 in the middle column (marked by arrows). Images in the same row are displayed with the same window and level settings.

In addition, the limited-angle DBT reconstruction causes interplane artifact in the depth direction (Z), and stronger in-plane artifact along the x-ray source motion direction (Y) than that along the direction perpendicular to the x-ray source motion direction (X). All these artifacts can affect the estimation of FWHM of the MCs. The blurring due to oblique incidence of the X-ray beam to the detector and to the slice of substantial thickness (1 mm in our study) for reconstruction is also much stronger in the Y-direction than in the X-direction. These factors may affect the FWHM estimation to different degrees for different speck sizes. We will investigate the impact of beam hardening and other factors on the sharpness of the MCs in future studies.

In the breast phantom, clusters of calcium carbonate specks were sandwiched between the slabs, which created an air gap. The nominal sizes of the specks ranged between 0.15 and 0.30 mm. The slice spacing in the depth (Z-) direction was 1 mm. The air gap might cause a small partial volume effect

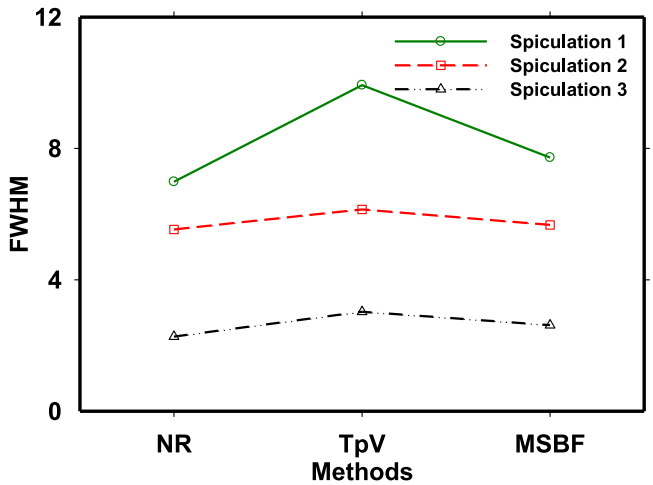

FIG. 15. Comparison of FWHM values on three different reconstruction methods for three spiculations in Fig. 14.

on the reconstructed voxels neighboring the air gap. Note that the breast phantom study was conducted to evaluate the dependence of the image quality of MCs on the MSBF parameters and the relative performances of the different regularization methods. Because the partial volume effect was present for all specks and under all reconstruction conditions, its impact, if any, on the relative performances and parameter selection should be minor.

5. CONCLUSION

The multiscale bilateral filtering regularization method for DBT reconstruction exploits the multiscale structure of image information in DBT. It is effective in suppressing noise, enhancing the visibility of MCs, and preserving the image quality of subtle spiculations. The effects of regularization on the image quality of MCs and spiculated masses were evaluated quantitatively using DBT images of breast phantoms and human subjects. The results demonstrate that the SART regularized by the MSBF method enhanced the CNR and preserved the sharpness of MCs. The MSBF method did not cause substantial blurring of spiculations compared to without regularization. It reduced *staircasing* artifacts on the regularized images, in contrast to the TpV method. The MSBF reconstruction has the potential to improve the CNR of MCs without compromising the image quality of masses and the soft tissue background structures in DBT.

ACKNOWLEDGMENTS

This work was supported by USPHS Grant No. RO1 CA151443. The digital breast tomosynthesis system was developed by the GE Global Research Group, with input and some revisions from the University of Michigan investigators, through the Biomedical Research Partnership (USPHS Grant No. CA91713, PI: Paul Carson, Ph.D.) collaboration. The content of this paper does not necessarily reflect the position of the funding agencies and no official endorsement of any equipment and product of any companies mentioned should be inferred.

[a]Author to whom correspondence should be addressed. Electronic mail: yaol@umich.edu; Telephone: (734) 647-8556; Fax: (734) 615-5513. Present address: Guangdong Province Key Laboratory of Computational Science, School of Mathematics and Computational Science, Sun Yat-sen University, Guangdong 510275, China.

[1]L. T. Niklason, B. T. Christian, L. E. Niklason, D. B. Kopans, D. E. Castleberry, B. H. Opsahl-Ong, C. E. Landberg, P. J. Slanetz, A. A. Giardino, R. Moore, D. Albagli, M. C. DeJule, F. C. Fitzgerald, D. F. Fobare, B. W. Giambattista, R. F. Kwasnick, J. Liu, S. J. Lubowski, G. E. Possin, J. F. Richotte, C. Y. Wei, and R. F. Wirth, "Digital tomosynthesis in breast imaging," Radiology **205**, 399–406 (1997).

[2]D. B. Kopans, "Novel approaches and newer imaging modalities," in *Course 815: Problem-solving Breast Imaging, RSNA Program Book* (RSNA, Chicago, 2001), p. 97.

[3]T. Wu, A. Stewart, M. Stanton, T. McCauley, W. Phillips, D. B. Kopans, R. H. Moore, J. W. Eberhard, B. Opsahl-Ong, L. Niklason, and M. B. Williams, "Tomographic mammography using a limited number of low-dose cone-beam projection images," Med. Phys. **30**, 365–380 (2003).

[4]D. B. Kopans, "Digital tomosynthesis and other applications," in *Categorical Course in Diagnostic Radiology: Breast Imaging-Digital Mammography, RSNA Program Book* (RSNA, Chicago, 2005), p. 130.

[5]M. A. Helvie, M. A. Roubidoux, Y. Zhang, P. L. Carson, and H.-P. Chan, "Tomosynthesis mammography vs conventional mammography: Lesion detection and reader preference. Initial experience," in *RSNA Program Book* (RSNA, Chicago, 2006), p. 335.

[6]M. A. Helvie, M. A. Roubidoux, L. M. Hadjiiski, Y. Zhang, P. L. Carson, and H.-P. Chan, "Tomosynthesis mammography vs conventional mammography: Comparison of breast masses detection and characterization," in *RSNA Program Book* (RSNA, Chicago, 2007), p. 381.

[7]S. P. Poplack, T. D. Tosteson, C. A. Kogel, and H. M. Nagy, "Digital breast tomosynthesis: Initial experience in 98 women with abnormal digital screening mammography," Am. J. Roentgenol. **189**, 616–623 (2007).

[8]I. Andersson, D. M. Ikeda, S. Zackrisson, M. Ruschin, T. Svahn, P. Timberg, and A. Tingberg, "Breast tomosynthesis and digital mammography: A comparison of breast cancer visibility and BIRADS classification in a population of cancers with subtle mammographic findings," Eur. Radiol. **18**, 2817–2825 (2008).

[9]G. Gennaro, E. Baldan, E. Bezzon, M. La Grassa, L. Pescarini, and C. di Maggio, "Clinical performance of digital breast tomosynthesis versus full-field digital mammography: Preliminary results," *Digital Mammography*, IWDM 2008-Lecture Notes in Computer Science Vol. 5116 (Springer, Berlin, 2008), pp. 477–482.

[10]M. A. Helvie, M. A. Roubidoux, L. M. Hadjiiski, Y. Zhang, P. L. Carson, and H.-P. Chan, "Research digital tomosynthesis mammography: Detection of T1 invasive breast carcinomas not diagnosed by conventional breast imaging or physical exam," in *RSNA Program Book* (RSNA, Chicago, 2008), p. 468.

[11]D. Gur, G. S. Abrams, D. M. Chough, M. A. Ganott, C. M. Hakim, R. L. Perrin, G. Y. Rathfon, J. H. Sumkin, M. L. Zuley, and A. I. Bandos, "Digital breast tomosynthesis: Observer performance study," Am. J. Roentgenol. **193**, 586–591 (2009).

[12]D. B. Kopans, "Digital breast tomosynthesis: Experience with imaging over 3500 subjects," in *Categorical Course in Diagnostic Radiology Physics: Advances in Digital Tomosynthesis—From Physics to Clinical Applications, RSNA Program Book* (RSNA, Chicago, 2009), p. 288.

[13]M. A. Helvie, H.-P. Chan, L. Hadjiiski, M. M. Goodsitt, M. A. Roubidoux, and P. L. Carson, "Digital breast tomosynthesis mammography: Effect of breast density on breast mass visibility and characterization," in *RSNA Program Book 2010 LL-BRS-WE* (RSNA, Chicago, 2010).

[14]H.-P. Chan, Y. T. Wu, B. Sahiner, J. Wei, M. A. Helvie, Y. Zhang, R. H. Moore, D. B. Kopans, L. Hadjiiski, and T. Way, "Characterization of masses in digital breast tomosynthesis: Comparison of machine learning in projection views and reconstructed slices," Med. Phys. **37**, 3576–3586 (2010).

[15]M. L. Spangler, M. L. Zuley, J. H. Sumkin, G. Abrams, M. A. Ganott, C. Hakim, R. Perrin, D. M. Chough, R. Shah, and D. Gur, "Detection and classification of calcifications on digital breast tomosynthesis and 2D digital mammography: A comparison," Am. J. Roentgenol. **196**, 320–324 (2011).

[16]T. M. Svahn, D. P. Chakraborty, D. Ikeda, S. Zackrisson, Y. Do, S. Mattsson, and I. Andersson, "Breast tomosynthesis and digital mammography: A comparison of diagnostic accuracy," Br. J. Radiol. **85**, E1074–E1082 (2012).

[17]M. G. Wallis, E. Moa, F. Zanca, K. Leifland, and M. Danielsson, "Two-view and single-view tomosynthesis versus full-field digital mammography: High-resolution x-ray imaging observer study," Radiology **262**, 788–796 (2012).

[18]E. A. Rafferty, J. M. Park, L. E. Philpotts, S. P. Poplack, J. H. Sumkin, E. F. Halpern, and L. T. Niklason, "Assessing radiologist performance using combined digital mammography and breast tomosynthesis compared with digital mammography alone: Results of a multicenter, multireader trial," Radiology **266**, 104–113 (2013).

[19]S. L. Rose, A. L. Tidwell, L. J. Bujnoch, A. C. Kushwaha, A. S. Nordmann, and R. Sexton, "Implementation of breast tomosynthesis in a routine screening practice: An observational study," Am. J. Roentgenol. **200**, 1401–1408 (2013).

[20]P. Skaane, A. I. Bandos, R. Gullien, E. B. Eben, U. Ekseth, U. Haakenaasen, M. Izadi, I. N. Jebsen, G. Jahr, and M. Krager, "Comparison of digital mammography alone and digital mammography plus tomosynthesis in a population-based screening program," Radiology **267**, 47–56 (2013).

[21]R. C. Gonzalez and R. E. Woods, *Digital image processing*, 2nd ed. (Prentice-Hall, 2002).

[22]P. Perona and J. Malik, "Scale-space and edge detection using anisotropic diffusion," IEEE Trans. Pattern Anal. Mach. Intell. **12**, 629–639 (1990).

[23]L. I. Rudin, S. Osher, and E. Fatemi, "Nonlinear total variation based noise removal algorithms," Phys. D (Amsterdam, Neth.) **60**, 259–268 (1992).
[24]M. Black, G. Sapiro, D. Marimont, and D. Heeger, "Robust anisotropic diffusion," IEEE Trans. Image Process. **7**, 421–432 (1998).
[25]D. Barash and D. Comaniciu, "A common framework for nonlinear diffusion, adaptive smoothing, bilateral filtering and mean shift," Image and Vision Comput. **22**, 73–81 (2004).
[26]B. Zhang and J. P. Allebach, "Adaptive bilateral filter for sharpness enhancement and noise removal," IEEE Trans. Image Process. **17**, 664–678 (2008).
[27]E. Y. Sidky, I. S. Reiser, R. Nishikawa, and X. C. Pan, "Image reconstruction in digital breast tomosynthesis by total variation minimization," Proc. SPIE **6510**, U1110–U1115 (2007).
[28]I. Kastanis, S. Arridge, A. Stewart, S. Gunn, C. Ullberg, and T. Francke, "3D digital breast tomosynthesis using total variation regularization," *Digital Mammography*, IWDM 2008-Lecture Notes in Computer Science Vol. 5116 (Springer, Berlin, 2010), pp. 621–627.
[29]E. Y. Sidky, X. Pan, I. Reiser, R. M. Nishikawa, R. H. Moore, and D. B. Kopans, "Enhanced imaging of microcalcifications in digital breast tomosynthesis through improved image-reconstruction algorithms," Med. Phys. **36**, 4920–4932 (2009).
[30]J. W. Garrett, W. I. Madison, J. Tang, E. S. Burnside, J. B. Garrett, and G.-H. Chen, "Dose reduction in digital breast tomosynthesis with prior image constrained compressed sensing (PICCS)," in *RSNA Program Book* (RSNA, Chicago, 2012).
[31]Y. Lu, H.-P. Chan, J. Wei, and L. M. Hadjiiski, "Selective-diffusion regularization for enhancement of microcalcifications in digital breast tomosynthesis reconstruction," Med. Phys. **37**, 6003–6014 (2010).
[32]Y. Lu, H.-P. Chan, J. A. Fessler, L. Hadjiiski, J. Wei, and M. M. Goodsitt, "Adaptive diffusion regularization for enhancement of microcalcifications in digital breast tomosynthesis (DBT) reconstruction," Proc. SPIE **7961**, 796117-1–796117-9 (2011).
[33]A. K. Jerebko, M. Kowarschik, and T. Mertelmeier, "Regularization parameter selection in maximum a posteriori iterative reconstruction for digital breast tomosynthesis," *Digital Mammography*, IWDM2010-Lecture Notes in Computer Science Vol. 6136 (Springer, Berlin, 2010), pp. 548–555.
[34]M. Das, H. C. Gifford, J. M. O'connor, and S. J. Glick, "Penalized maximum likelihood reconstruction for improved microcalcification detection in breast tomosynthesis," IEEE Trans. Med. Imaging **30**, 904–914 (2011).
[35]Y. Lu, H.-P. Chan, J. Wei, L. M. Hadjiiski, and C. Zhou, "Multiscale regularized reconstruction for enhancing microcalcification in digital breast tomosynthesis," Proc. SPIE **8313**, 831322-1–831322-9 (2012).
[36]Y. Lu, H.-P. Chan, J. Wei, R. K. Samala, L. Hadjiiski, and P. L. Carson, "Multiscale bilateral regularization in digital breast tomosynthesis (DBT)," in *RSNA Program Book SSE22* (RSNA, Chicago, 2012).
[37]A. Kak and M. Slaney, *Principle of Computerized Tomographic Imaging* (IEEE, 1988).
[38]Y. Zhang, H.-P. Chan, B. Sahiner, J. Wei, M. M. Goodsitt, L. M. Hadjiiski, J. Ge, and C. Zhou, "A comparative study of limited-angle cone-beam reconstruction methods for breast tomosynthesis," Med. Phys. **33**, 3781–3795 (2006).
[39]R. L. Siddon, "Fast calculation of the exact radiological path for a three-dimensional CT array," Med. Phys. **12**, 252–255 (1985).
[40]T. Wu, R. H. Moore, E. A. Rafferty, and D. B. Kopans, "A comparison of reconstruction algorithms for breast tomosynthesis," Med. Phys. **31**, 2636–2647 (2004).
[41]M. Jiang and G. Wang, "Convergence of the simultaneous algebraic reconstruction technique (SART)," IEEE Trans. Image Process. **12**, 957–961 (2003).
[42]P. J. Burt and E. H. Adelson, "The Laplacian pyramid as a compact image code," IEEE Trans. Commun. **31**, 337–345 (1983).
[43]H.-P. Chan, S. C. B. Lo, L. T. Niklason, D. M. Ikeda, and K. L. Lam, "Image compression in digital mammography: Effects on computerized detection of subtle microcalcifications," Med. Phys. **23**, 1325–1336 (1996).
[44]S. Dippel, M. Stahl, R. Wiemker, and T. Blaffert, "Multiscale constrast enhancement for radiographies: Laplacian pyramid versus fast wavelet transform," IEEE Trans. Med. Imaging **21**, 343–353 (2002).
[45]J. Wei, B. Sahiner, L. M. Hadjiiski, H.-P. Chan, N. Petrick, M. A. Helvie, M. A. Roubidoux, J. Ge, and C. Zhou, "Computer aided detection of breast masses on full field digital mammograms," Med. Phys. **32**, 2827–2838 (2005).
[46]A. S. Saad, "Simultaneous speckle reduction and contrast enhancement for ultrasound images: Wavelet versus Laplacian pyramid," Pattern Recognit. Image Anal. **18**, 63–70 (2008).
[47]X. Liu, J. Tang, S. Xiong, Z. Feng, and Z. Wang, "A multiscale contrast enhancement algorithm for breast cancer detection using Laplacian Pyramid," in *Proceedings of International Conference on Information and Automation* (IEEE, New York, 2009), p. 1167–1171.
[48]C. Tomasi and R. Manduchi, "Bilateral filtering for gray and color images," in *Proceedings of Sixth International Conference on Computer Vision* (IEEE, New York, 1998), p. 839–846.
[49]S. M. Smith and J. M. Brady, "SUSAN—A new approach to low level image processing," Int. J. Comput. Vision **23**, 45–78 (1997).
[50]N. Sochen, R. Kimmel, and R. Malladi, "A general framework for low level vision," IEEE Trans. Image Process. **7**, 310–318 (1998).
[51]J. Van de Weijer and R. Van den Boomgaard, "Local mode filtering," in *Proceedings of Computer Vision and Pattern Recognition* (IEEE, New York, 2001), Vol. 2, p. 428–433.
[52]M. Elad, "On the origin of the bilateral filter and ways to improve it," IEEE Trans. Image Process. **11**, 1141–1151 (2002).
[53]D. Barash, "Fundamental relationship between bilateral filtering, adaptive smoothing, and the nonlinear diffusion equation," IEEE Trans. Pattern Anal. Mach. Intell. **24**, 844–847 (2002).
[54]J. Chen, S. Paris, and F. Durand, "Real-time edge-aware image processing with the bilateral grid," ACM Trans. Graphics **26**, 103 (pp. 1–10) (2007).
[55]R. Fattal, M. Agrawala, and S. Rusinkiewicz, "Multiscale shape and detail enhancement from multi-light image collections," ACM Trans.Graphics **26**, 51 (pp. 1–9) (2007).
[56]M. Zhang and B. K. Gunturk, "Multiresolution bilateral filtering for image denoising," IEEE Trans.Image Process. **17**, 2324–2333 (2008).
[57]H.-P. Chan, M. M. Goodsitt, M. A. Helvie, S. Zelakiewicz, A. Schmitz, M. Noroozian, C. Paramagul, M. A. Roubidoux, A. V. Nees, C. Neal, P. L. Carson, Y. Lu, L. M. Hadjiiski, and J. Wei, "Digital breast tomosynthesis: Observer performance study the detection clustered microcalcifications breast phantom images acquired with experimental DBT system using variable scan angles angular increments, and number of projection views," Radiology **273**, 675–685 (2014).
[58]P. Blomgren, T. F. Chan, P. Mulet, L. Vese, and W.-L. Wan, *Variational PDE Models and Methods for Image Processing*, Numerical Analysis 1999 (Chapman & Hall/CRC, New York, 2000).
[59]V. Bustamante, "Iterative polyenergetic digital tomosynthesis reconstructions for breast Cancer screening," Ph.D. thesis, 2013.
[60]Y. Lin and E. Samei, "An efficient polyenergetic SART (pSART) reconstruction algorithm for quantitative myocardial CT perfusion," Med. Phys. **41**, 021911 (14pp.) (2014).
[61]Y. Lin and E. Samei, "A fast poly-energetic iterative FBP algorithm," Phys. Med. Biol. **59**, 1655–1678 (2014).